East European Journal of Physics. 1. 79-90 (2025)
DOI:10.26565/2312-4334-2025-1-07 ISSN 2312-4334

EIGEN RADIO FREQUENCY SIGNALS LOCALIZED AT ALFVEN RESONANCES IN A TOKAMAK SCRAPE-OFF LAYER

I. Girka[a]*, O. Trush[a], W. Tierens[b]
[a]*V.N. Karazin Kharkiv National University, Kharkiv, Ukraine*
[b]*Oak Ridge National Laboratory, Oak Ridge, USA*
**Corresponding Author e-mail: igor.girka@ipp.mpg.de*
Received December 12, 2024; revised January 3, 2025; accepted February 1, 2025

Eigen electromagnetic waves with small toroidal wave indices and positive poloidal wave indices are considered in the Ion Cyclotron Range of Frequencies (ICRF) in a tokamak Scrape-Off Layer (SOL). The waves are shown theoretically to exist in the form of the signals localized at the local Alfven Resonances (ARs). The evanescent regions in the direction of lower plasma density are provided by the presence of the wave nonzero poloidal wave indices. The narrow evanescent regions in the direction of higher plasma density are caused by strong plasma variation. The latter regions separate ARs from the high-density SOL and plasma core which are propagating regions for ICRF waves. The dispersion relation of ICRF signals is derived analytically and solved numerically. Possible relevance of the obtained results to experimental measurements is discussed. An exhaustive definition of the signals' excitation sources is out of scope of the present study.
Keywords: *Eigen waves; Ion cyclotron range of frequencies; Alfven resonance; Tokamak scrape-off layer; Asymptotic methods; Dispersion relation*
PACS: 52.35.Bj

INTRODUCTION

Alfven Waves (AWs) were predicted by Hannes Alfven more than eighty years ago [1]. Soon they were experimentally observed by Allen with co-authors [2]. Since then, AWs are extensively studied due to multiple practical applications, in particular, in fusion plasmas and astrophysics.

Plasma non-uniformity both in a laboratory and nature forms preconditions for the propagation of various AW types. For instance, elliptical shape of the fusion device cross-section was shown in [3] to give rise to eigen ellipticity induced Alfven waves (EAEs). AWs with zero toroidal mode number were observed, e.g., in the ellipticity-induced frequency range in JET [4]. Toroidal periodic non-uniformity of fusion plasmas gives rise to toroidal Alfvén eigenmodes (TAEs). An enlarged spectrum of ideal TAEs was demonstrated to exist within a toroidicity-induced Alfvén gap in [5]. Following the experimental observations of TAEs in a counter-current Neutral Beam Injection (NBI) scenario developed in TCV, an in-depth analysis of the impact of such modes on the global confinement and performance was carried out in [6].

The presence of the so-called non-axisymmetric resonances of wave-particle interaction in stellarators which are associated with the lack of axial symmetry of the magnetic configuration were found in [7] to have a strong stabilizing influence through Landau mechanism on TAEs destabilized by the energetic ions. Thermal ions were also reported in [7] to interact with high frequency Alfvén gap modes (helicity-induced Alfvén Eigenmodes and mirror-induced Alfvén Eigenmodes), leading to a considerable damping of these modes at the high pressure attributed to, e.g., a Helias reactor.

Physics of the transverse energy transfer by Alfvén waves in toroidal plasmas was elucidated in [8]. In contrast to the classical Alfvén waves in infinite plasmas, the Alfvén waves in toroidal systems were found to produce plasma compression due to coupling with fast magnetoacoustic waves with providing the energy transfer. The radial group velocities of the traveling waves constituting the Global Alfvén Eigenmodes and TAEs were calculated. The obtained results were applied to explain how Alfvén eigenmodes could provide the spatial energy channeling - the transfer of the energy by these modes from the unstable plasma region to the region where the mode damping dominated.

Non-linear dynamics of multiple infernal Alfvén eigenmodes—a subset of global Alfvén eigenmodes in tokamak plasmas with extended low-shear central core was studied in [9]. The analysis was carried out for a mode triplet with toroidal mode-numbers n = 1, 2, 3. The temporal evolution of the amplitudes and the phase (responsible for the frequency chirping) of the modes was found to exhibit Hopf bifurcations to stable limit cycles. This conclusion was applied for explanation of a synchronous cyclic destabilization of multiple modes in Alfvén avalanches (sudden growth of amplitudes of the mode cluster with different n and approximately equal frequency spacing) in NSTX and bursting modes in MAST.

Comprehensive overview of studying AWs at Institute of Plasma Physics in Kharkiv including the research carried out in collaboration with the research centers of Sweden, Belgium, United Kingdom and Germany was presented in [10]. In particular, various types of Alfvén eigenmodes (AEs) were reported in [11] to be destabilized by fast ions over a broad frequency range in a series of JET experiments in mixed D–3He plasmas. The radial localization of AEs was identified using an X-mode reflectometer, a multiline interferometer and soft x-ray diagnostics. Two different types of Alfvén cascade (AC) eigenmodes were observed originating from the presence of a local minimum of the safety factor. In addition

Cite as: I. Girka, O. Trush, W. Tierens, East Eur. J. Phys. 1, 79 (2025), https://doi.org/10.26565/2312-4334-2025-1-07
© I. Girka, O. Trush, W. Tierens, 2025; CC BY 4.0 license

to ACs with frequencies below the frequency of TAEs, ACs with frequencies above the TAE frequency were destabilized by energetic ions. Both ACs were localized in the central regions of the plasma.

The deuterium ions accelerated to MeV range in three-ion radio frequency scenario of NBI were shown in [12,13] to produce fusion-born alpha-particles from the D-3He reaction. These alpha-particles were reported to excite EAEs with toroidal mode indices n = −1 and n = 0. The fusion-born alpha-particles rather than accelerated D-ions were shown to interact with EAEs with negative toroidal mode indices. The n = 0 EAEs were found to be excited only if a fast-ion population energy distribution had so-called 'bump-on-tail distribution (where $\partial f/\partial E > 0$).

The identification of TAEs at different radial locations in counter-current NBI scenarios in TCV was presented in [14]. These modes were reported to be significantly different from the ones observed previously in scenarios with co-current off-axis NBI and electron cyclotron heating.

Fourier analyses of the fast-ion loss detector revealed coherent fast-ion losses in the range of the 1...2 MHz in MAST-U [15]. The losses were found to correlate with modes identified as Compressional and Global Alfvén Eigenmodes by the Mirnov coils.

Local Alfven resonance (AR) as a method of plasma heating was first studied in [16]. Comprehensive overview of theoretical research of plasma Alfven heating was presented in [17]. ARs were effectively applied for plasma production and heating in various fusion devices (see, e.g., [18,19]). However, position of ARs is well-known to move to the plasma edge with increase in plasma density which reduces the efficiency of Alfven method of plasma heating and its application for these purposes in modern experiments. Comprehensive overview of the recent studies of AWs and plasma Alfven heating was given e.g. in [20].

Excitation of surface waves with $|k_z| < k_0$ and $\omega > \omega_{ci}$ within Alfven resonance regions by ICRF antenna was numerically demonstrated in [21] with focusing on the cases of DEMO and ITER (here k_z is toroidal wavenumber, k_0 is vacuum wavenumber, $k_0 = \omega/c$, ω is the wave angular frequency, ω_{ci} is ion cyclotron frequency, and c is the speed of light in vacuum). The fast wave field spatial distribution was obtained by the semi-analytic code ANTITER II in plane geometry by summation of Fourier series over the toroidal and poloidal wave indices. A few well radially separated standing (in toroidal direction) wave patterns in edge plasma were clearly demonstrated. This is different from what was is discussed in the present paper. The difference is explained by the fact that the present paper studies the problem of eigen functions and eigen values rather than that of forced oscillations as it was in [21].

In the present paper, the possibility for eigen ICRF signal to be localized in the vicinity of the local AR

$$S \equiv 1 - \frac{\omega_{pi}^2}{\omega^2 - \omega_{ci}^2} = N_z^2, \tag{1}$$

is shown. In (1), S is the component of cold plasma permittivity tensor in Stix notations [22], $N_z = k_z/k_0$ is toroidal refractive index, and ω_{pi} is ion plasma frequency. The wave field spatial distribution is found analytically in the vicinity of the resonance. The distribution corresponds to the localized ICRF signal: the fields decay exponentially with distance from AR (1), both towards the low-density and the high-density plasma. The dispersion relation is analyzed numerically by means of the standard package "Wolfram Mathematica", version 13.1 [23]. Relevance of the numerical results to possible experimental observations is discussed.

The novelty of the present paper is associated with three issues. First, previous analytical studies of AR fine structure were carried out in the framework of models with linear plasma density variation. This assumption was proved by small scale of kinetic and inertial Alfven waves into which large scale magnetohydrodynamic waves converted within ARs. However, plasma density profile in a tokamak SOL can be modelled as exponential decay with the distance from the plasma core. Sufficiently small decay length makes the search of the wave field spatial distribution out of ARs analytically tractable which is realized in the present paper.

Second, no evanescent layer exists between ARs and high-density plasma in the case of smooth plasma density variation and moderate poloidal wave indices. Existence of the layer is the necessary precondition for the ICRF signal localized spatial distribution. Strong exponential variation of the plasma density in a tokamak SOL causes the existence of the layer.

Third, previous studies (analytical and also many of numerical) were carried out with neglecting the toroidal (parallel to external static magnetic field) wave electric field E_z. This is correct due to sufficiently large absolute value of the plasma permittivity component ε_{zz} (P in Stix notations applied below) in ICRF. This issue made it possible to significantly simplify the analysis by reducing Maxwell's system of equations within ARs to the second order ordinary uniform differential equation. Presence of the evanescent layer for E_z between an antenna and ARs causes decay of forced E_z falling on ARs from the antenna side. However, in the case of eigen waves, the same evanescent layer causes decay of E_z with the distance in opposite direction: from ARs to the metal wall. This results in the necessity to consider coupled electromagnetic waves within ARs described by two coupled second order ordinary nonuniform differential equations. These two coupled equations are solved in the present paper to determine the wave field spatial distribution within ARs.

The paper is arranged as follows. The theoretical model is reported in section II with the emphasis on the SOL separation into four regions within which different asymptotic solutions can be applied. Wave field spatial distribution is presented in section III. The dispersion relation is given in section IV. The results of the numerical study of the dispersion properties are presented in section V. The main conclusions and discussions are found in section VI.

II. MODEL DESCRIPTION

The SOL is considered in slab geometry with x axis being perpendicular to the SOL and directed from the low-density to the high-density plasma (opposite to the radial direction). External static uniform magnetic field $\vec{B}_0$ is parallel to the SOL and directed along z axis, $\vec{B}_0||\vec{z}$. SOL is assumed to be uniform along y axis which is chosen such that x, y and z axes form the right triple of vectors (Fig. 1). Plasma electrodynamic properties are described in terms of cold collisionless plasma dielectric permittivity tensor (in Stix notations [22]):

$$\hat{\varepsilon}(x) = \begin{pmatrix} S & -iD & 0 \\ iD & S & 0 \\ 0 & 0 & P \end{pmatrix}. \tag{2}$$

Within the ion cyclotron frequency range, $\omega_{ci} < \omega \ll |\omega_{ce}|$, the tensor components read

$$S = 1 - \frac{\omega_{pi}^2}{\omega^2 - \omega_{ci}^2},\ D = \frac{\omega_{pi}^2 \omega}{\omega_{ci}(\omega^2 - \omega_{ci}^2)},\ P = 1 - \frac{\omega_{pe}^2}{\omega^2}. \tag{3}$$

Hereinafter, ω_{ce} is electron cyclotron frequency, and ω_{pe} is electron plasma frequency.

The wave field spatial distribution is to be found in the form of Fourier harmonic, e.g., the wave toroidal magnetic field

$$\tilde{H_z}(\vec{r}, t) = H_z(x)\exp\left[i\left(k_z z + k_y y - \omega t\right)\right]. \tag{4}$$

In (4), k_y is poloidal wavenumber. Then the wave amplitudes $E_z(x)$ and $H_z(x)$ spatial distribution is governed by two coupled second order ordinary linear differential equations:

$$\frac{1}{k_0^2}\frac{d^2E_z}{dx^2} + \frac{N_z^2}{k_0^2}\frac{d}{dx}\left(\frac{1}{N_\perp^2}\frac{dE_z}{dx}\right) + \frac{N_z^2 N_y}{k_0}E_z\frac{d}{dx}\left(\frac{\mu}{N_\perp^2}\right) + E_z\left[P - N_y^2 - \frac{N_z^2 N_y^2}{N_\perp^2}\right] = -\frac{iN_z}{k_0^2}\frac{d}{dx}\left(\frac{\mu}{N_\perp^2}\frac{dH_z}{dx}\right) - \frac{iN_z N_y}{k_0}H_z\frac{d}{dx}\left(\frac{1}{N_\perp^2}\right) + \frac{iN_z N_y^2 \mu}{N_\perp^2}H_z, \tag{5}$$

$$\frac{1}{k_0^2}\frac{d}{dx}\left(\frac{1}{N_\perp^2}\frac{dH_z}{dx}\right) + H_z\left[1 - \frac{N_y^2}{N_\perp^2} + \frac{N_y}{k_0}\frac{d}{dx}\left(\frac{\mu}{N_\perp^2}\right)\right] = \frac{i}{k_0^2}\frac{d}{dx}\left(\frac{\mu N_z}{N_\perp^2}\frac{dE_z}{dx}\right) - \frac{iN_y^2}{N_\perp^2}\mu N_z E_z + \frac{iN_z N_y}{k_0}E_z\frac{d}{dx}\left(\frac{1}{N_\perp^2}\right). \tag{6}$$

In (5), and (6), $N_y = k_y/k_0$ is poloidal refractive index, $\mu = -D/(S - N_z^2)$, $N_\perp^2 = (R - N_z^2)(L - N_z^2)/(S - N_z^2)$, $R = S + D$, and $L = S - D$.

To derive the dispersion relation, one needs also the expressions for y-components of electrical and magnetic wave fields:

$$E_y = \frac{-1}{N_\perp^2}\{\frac{i}{k_0}\frac{dH_z}{dx} + N_z N_y E_z + \mu[iN_y H_z + \frac{N_z}{k_0}\frac{dE_z}{dx}]\}, \tag{7}$$

$$H_y = \frac{-N_z}{N_\perp^2}\left\{N_y H_z - \frac{iN_z}{k_0}\frac{dE_z}{dx} + \mu\left[-iN_y N_z E_z + \frac{1}{k_0}\frac{dH_z}{dx}\right]\right\} + \frac{i}{k_0}\frac{dE_z}{dx}. \tag{8}$$

These tangential components should be continuous at the interfaces between the regions specified below.

Plasma particle density is assumed to increase exponentially within the SOL [24],

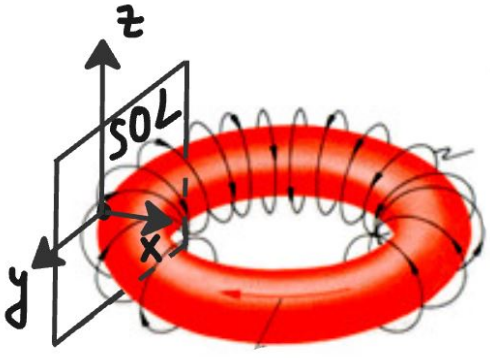

Figure 1. Schematic of the problem

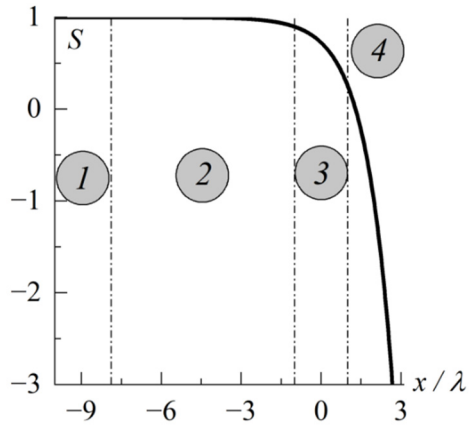

Figure 2. Spatial variation of $S(x)$ (solid curve) and within the low-density SOL. Numbers 1-4 in grey circles indicate the four regions, into which the SOL is separated to make the Maxwell's equations analytically solvable. Dash-dotted vertical lines separate the regions. $n = 3$, $\omega/\omega_{ci} = 5.308$, $R = 2.12\ m$, $\lambda = 0.018\ m$, $B_0 = 2.0\ T$, $n(0) = 8.287 \times 10^{16}\ m^{-3}$)

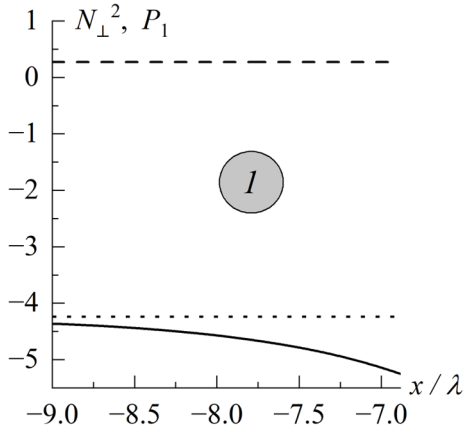

Figure 3. Spatial variation of $N_\perp^2(x)$ (dashed curve), and $P_1(x)$ (solid curve) within the first region. Dotted line corresponds to vacuum value of P_1. The wave and plasma parameters are the same as in Fig. 2

$$n(x) = n_0 \exp\,(x/\lambda). \tag{9}$$

In (9), λ is the decay length, and n_0 is plasma density at $x = 0$ which is considered hereinafter as the position of the local resonance (1). It is the smallness of λ as compared with the tokamak plasma minor radius a which justifies the application of the slab geometry in the present paper, since the studied ICRF signal is shown hereinafter to be localized within the layer with the width of the order of λ.

The components S, D, P (3) of the plasma permittivity tensor, as well as coefficients in Maxwell's equations (5)-(8) vary significantly in low-density SOL. Separation of the SOL into four regions (Fig. 2) according to correlation between the components S, D, and P is explained below. Analytical asymptotic solutions of Eqs. (5)-(6) within these four regions are derived in the next section. The following wave and plasma parameters are applied while calculating the curves in Figs. 2-6: Deuterium single charged ions, toroidal wave index $n = 3$, ratio of the wave frequency to ion cyclotron frequency $\omega/\omega_{ci} = 5.308$, major plasma radius $R = 2.12\ m$, minor plasma radius $a = 0.5\ m$, density decay length $\lambda = 0.018\ m$, the external static uniform magnetic field $B_0 = 2.0\ T$, the plasma density $n(0) = 8.287 \times 10^{16}\ m^{-3}$, and the ion temperature of $T_i = 10.0\ eV$. The electron-ion collision frequency can be estimated for these plasma parameters as $\overline{\nu_{ei}} = 114.0\ kHz$ which is much smaller than ion cyclotron frequency $f_{ci} \approx 14.6\ MHz$. This fact confirms the validity of the collisionless plasma approximation applied in the present paper.

The **first region** (Fig. 3) is determined by the condition that the plasma density is sufficiently small there to provide so-called vacuum conditions:

$$|S - 1| \ll 1, |D| \ll 1, |P - 1| \ll 1. \tag{10}$$

In this region, the wave field spatial distribution can be determined precisely. The wave amplitude is assumed to decay exponentially with the distance from AR (1), $x \to -\infty$. The right boundary x_1 of the first region is determined as

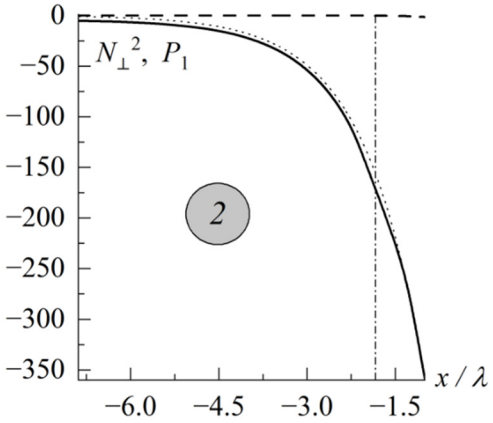

Figure 4. Spatial variation of $N_\perp^2(x)$ (dashed curve), and $P_1(x)$ (solid curve) within the second region. Thin dotted curve demonstrates the asymptotic $P(x)-1$ of $P_1(x)$. Thin vertical dash-dotted line indicates the position of $N_\perp^2(x)=0$. The wave and plasma parameters are the same as in Fig. 2

follows. The factor $P_1 \equiv P - N_y^2 - N_z^2 N_y^2/N_\perp^2$ placed in square brackets in eq. (5) transfers in the vicinity of x_1 from the value $1 - N_y^2 - N_z^2 N_y^2/(1-N_z^2)$, which is inherent for the vacuum, to $P-1$, which is the asymptotic for the larger plasma density, $|P-1| \gg (N_y^2 + N_z^2 - 1)/(1-N_z^2)$:

$$x_1 = \lambda \ln\left(\frac{m_e}{m_i}\frac{\omega^2}{\omega_{ci}^2}\frac{1}{N_A^2(0)}\right). \tag{11}$$

The factor P_1 is shown in Fig. 3 by solid curve. Its maximum deviation from the value $1 - N_y^2 - \frac{N_z^2 N_y^2}{1-N_z^2} \approx -4.237$ given in Fig. 3 by dotted line is observed at $x = x_1$: $P_1(x_1) \approx -5.241$. $N_\perp^2(x)$ is shown in Fig. 3 by dashed curve. It weakly deviates from its vacuum value $N_\perp^2(x \to -\infty) = 1 - N_z^2 \approx 0.276$. Even at the right boundary of the first region, the deviation is smaller than 10^{-4}.

Within the **second region** (Fig. 4), one can neglect plasma particle density, $\omega_{pi}^2 \to 0$, in the expressions for S and D; and must take the difference between P and a unit into account, $|P| \neq 1$. Neglecting the existence of this region would block searching for the solution to the dispersion relation. Comparison of $P_1(x)$ (solid curve in Fig. 4) with its asymptotic $P(x)-1$ presented by thin dotted curve justifies approach to solving eq. (5) presented below. Vertical dash-dotted line indicates the coordinate where $N_\perp^2(x)$ turns to zero and hence, $P_1(x)$ diverges. This divergence is not shown in Fig. 4. Wave fields are known to vary weakly in the vicinity of this coordinate.

The ICRF signal is expected to be localized in the **third region**, where $S \approx N_z^2$ (Fig. 5). Its boundaries can to be determined as follows:

$$-\lambda < x < +\lambda. \tag{12}$$

At the left boundary of the third region, the plasma particle density is sufficiently small to provide the following strong inequalities:

$$|S(-\lambda) - 1| \ll 1, |D(-\lambda)| \ll 1. \tag{13}$$

However, the absolute value of P is already large there, $|P(-\lambda)| \gg 1$. In the particular case, presented in Fig. 5, these quantities are equal: $S(-\lambda) - 1 \approx -0.102$, $D(-\lambda) \approx -0.539$, and $P(-\lambda) \approx -358.543$.

At the right boundary of the third region, the plasma density is sufficiently high, so that μ is almost uniform, $\mu(\lambda) \approx \omega/\omega_{ci}$, and $N_\perp^2$ behaves almost as Alfven refractive index squared, $N_\perp^2(\lambda) \approx N_A^2(\lambda)$ with $N_A \equiv \omega_{pi}/\omega_{ci}$. In the particular case, presented in Fig. 5, $\mu(\lambda) \approx 8.397$, $\omega/\omega_{ci} \approx 5.308$, $N_\perp^2(\lambda) \approx 32.978$, and $N_A^2(\lambda) \approx 20.395$.

The **fourth region** (Fig. 6) lies to the right of the third region,

$$x > +\lambda. \tag{14}$$

In this region, the wave is assumed to decay with the distance from the resonance (1), $x \to +\infty$. The latter boundary condition along with that for $x \to -\infty$ mentioned above provides the localized nature of the ICRF signal under the consideration. Physical essence of the mathematical condition $x \to +\infty$ is that the wave field amplitude decays

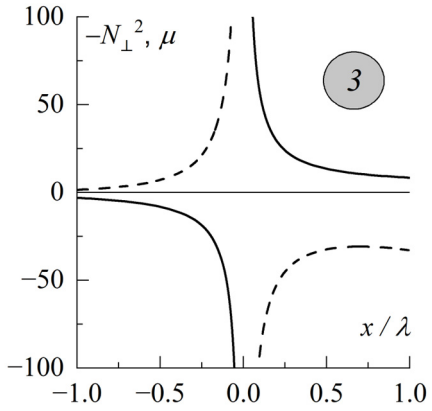

Figure 5. Spatial variation of $\mu(x)$ (solid curve) and $-N_\perp^2(x)$ (dashed curve) within the third region. The wave and plasma parameters are the same as in Fig. 2.

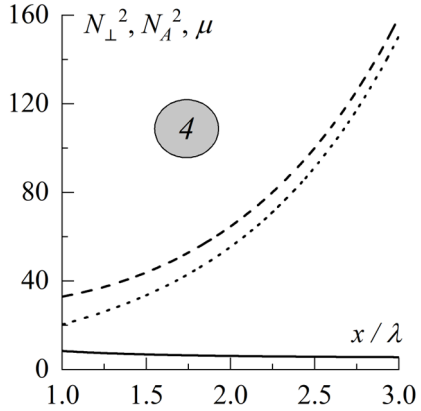

Figure 6. Spatial variation of $\mu(x)$ (solid curve), $N_\perp^2(x)$ (dashed curve), and $N_A^2(x)$ (dotted curve) within the fourth region. The wave and plasma parameters are the same as in Fig. 2

sufficiently before the fast wave reaches the region of its propagation in the high-density plasma. It should be underlined that the $N_\perp^2$ variation in the fourth region approximately follows that of the plasma particle density (9),

$$N_\perp^2 \approx N_A^2(0)\exp(x/\lambda). \tag{15}$$

The latter circumstance significantly simplifies searching the analytical (though approximate) solution to the Maxwell's equations in this region. Note also that μ weakly varies in this region, $\mu \approx \omega/\omega_{ci}$. Weak difference between $N_\perp^2$ and N_A^2 within the fourth region is clearly seen in Fig. 6 where these quantities are shown by dashed and dotted curves respectively. The solid curve in Fig. 6 confirms negligible variation of μ within the fourth region.

III. WAVE FIELD SPATIAL DISTRIBUTION

Within the first region, $-\infty < x < x_1$, both wave field amplitudes $E_z(x)$ and $H_z(x)$ are governed by the same second order uniform differential equations

$$\frac{d^2H_z}{dx^2} + \left(k_0^2 - k_y^2 - k_z^2\right)H_z = 0. \tag{16}$$

Their solutions, which satisfy the boundary condition of the wave field vanishing at $x \to -\infty$, read:

$$H_z = A_1\exp(k_1x),\ E_z = B_1\exp(k_1x). \tag{17}$$

In (17), A_1 and B_1 are the constants of integration, $k_1 = \sqrt{k_y^2 + k_z^2 - k_0^2}$ is assumed to be real observable which physical sense is as follows. The value k_1^{-1} is the spatial scale at which the wave field amplitude decreases by the factor of e. The dependences $E_z(x)$ and $H_z(x)$ within the first region are demonstrated in Fig. 7 by dashed and solid curves respectively to the left of $x_1 \approx -6.885\lambda$. For the plasma parameters applied in calculations for Fig. 7, $k_1 \approx 1.799\ m^{-1}$ is rather small, however, for the wave with $m = 5$, $k_1 \approx 6.0\ m^{-1}$.

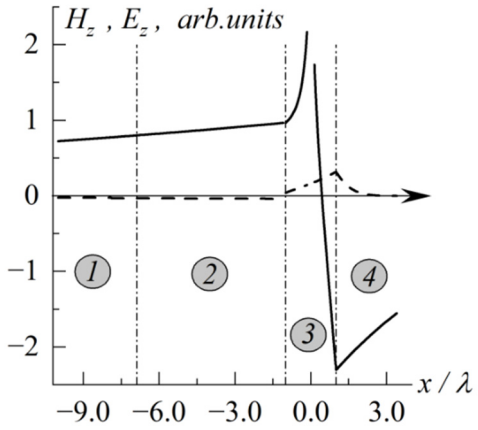

Figure 7. Wave field radial distribution: $H_z(x)$ – solid curves, $E_z(x)$ – dashed curves, $n = 3$, $m = 1$, other data is given in Section V. Vertical dash-dotted lines indicate the boundaries between the regions 1÷4

Within the second region, $x_1 < x < -\lambda$, the wave toroidal magnetic field spatial distribution is governed by the same equation (16) as in the first region unlike that of the wave toroidal electric field which is governed by the following truncated equation:

$$\frac{1}{k_0^2}\frac{d^2E_z}{dx^2} + (P-1)(1-N_z^2)E_z = 0. \tag{18}$$

The solution of eq. (18) can be written in terms of modified Bessel function $I_0(q)$ and McDonald function $K_0(q)$ of the zeroth order:

$$E_z = B_{21}I_0\left(2k_0\lambda\sqrt{(P-1)(N_z^2-1)}\right) + B_{22}K_0\left(2k_0\lambda\sqrt{(P-1)(N_z^2-1)}\right). \tag{19}$$

For the plasma parameters applied in calculations for Fig. 7, the Bessel function arguments in eq. (19) read $0.984\exp(0.5x/\lambda)$.

Within the third region, $-\lambda < x < +\lambda$, one applies the method of narrow layer [16,25] which is generalized in the present report for solving the set of two coupled second order differential equations. Summarizing in brief, the method of narrow layer is appropriate to be applied in the cases opposite to those when the WKB method is applicable one. The wave field spatial distribution within the third region reads

$$H_z = A_{31}\left\{1 - \int_{-\lambda}^{x}[(x+\lambda)k_\perp^2]dx + N_y^2\int_{-\lambda}^{x}\left[k_\perp^2\int_{-\lambda}^{x}\frac{dx}{N_\perp^2}\right]dx - k_y\int_{-\lambda}^{x}\mu dx\right\} - A_{32}\frac{1}{1-N_z^2}\int_{-\lambda}^{x}N_\perp^2 dx$$

$$+iB_{31}\left\{k_zN_y(x+\lambda) - N_y^2N_z\int_{-\lambda}^{x}\left[k_\perp^2\int_{-\lambda}^{x}\frac{\mu dx}{N_\perp^2}\right]dx - \frac{N_zk_y}{1-N_z^2}\int_{-\lambda}^{x}N_\perp^2dx\right\} + iB_{32}N_z\int_{-\lambda}^{x}\mu dx, \tag{20}$$

$$E_z = iA_{31}\left\{N_zk_y^2\int_{-\lambda}^{x}\left[\frac{1}{Q}\int_{-\lambda}^{x}\frac{\mu dx}{N_\perp^2}\right]dx - k_zN_y\int_{-\lambda}^{x}\frac{dx}{QN_\perp^2} + \frac{k_zN_y}{1-N_z^2}\int_{-\lambda}^{x}\frac{dx}{Q}\right\} - iA_{32}N_z\int_{-\lambda}^{x}\frac{\mu dx}{QN_\perp^2}$$

$$+B_{31}\left\{1 - N_z^2k_y\int_{-\lambda}^{x}\frac{\mu dx}{QN_\perp^2} - k_0^2\int_{-\lambda}^{x}\left[\frac{1}{Q}\int_{-\lambda}^{x}\left(P - N_y^2 - \frac{N_z^2N_y^2}{N_\perp^2}\right)dx\right]dx\right\} + B_{32}\frac{1}{1-N_z^2}\int_{-\lambda}^{x}\frac{dx}{Q}. \tag{21}$$

In (20), and (21), the constants of integration A_{31}, A_{32}, B_{31} and B_{32} have clear physical essence. They represent the wave field amplitudes and their derivatives at the left boundary of the region, $x = -\lambda$:

$$A_{31} = H_z(-\lambda),\ A_{32} = \frac{dH_z}{dx}_{|x=-\lambda},\ B_{31} = E_z(-\lambda),\ B_{32} = \frac{dE_z}{dx}_{|x=-\lambda}. \tag{22}$$

In (20), and (21), the following notation is applied

$$Q = \frac{D^2 - S(S-N_z^2)}{D^2 - (S-N_z^2)^2}. \tag{23}$$

The most important benefit from application of Eqs. (20) and (21) is that they connect the values of the wave fields at the opposite sides of the resonance (1).

The problem of electromagnetic energy absorption in the vicinity of the resonance (1) is out of scope of the present paper. Consequently, the wave field distribution shown in Fig. 7 within the third region is discontinuous: no data is presented for $-0.147\lambda < x < 0.147\lambda$. The figure 0.147 corresponds to the characteristic local resonance width, $\Delta x \sim (\rho_{Li}^2 \lambda)^{\frac{1}{3}} \approx 5.3 \times 10^{-3}\ m$ [16,26,27] (here ρ_{Li} is ion Larmor radius). Exclusion of this interval of coordinates from the consideration results in absence of evident resonant behavior of the wave electric field E_z unlike the wave magnetic field H_z which demonstrates resonant growth with approaching to the coordinate $x = 0$. The absence of E_z resonant behavior in Fig. 7 can be explained by different type of the wave field singularity in the cold plasma approximation, in which $H_z \propto \ln|S - N_z^2|$ and $E_z \propto (S - N_z^2)^{-2}$ which means that the resonance of E_z is narrower than that of H_z.

One can note different nature of $H_z(x)$ dependence on opposite sides of the resonant point $x = 0$ presented in Fig. 7. The wave field $H_z(x)$ decays with distance from $x = 0$ to the left ($x < 0$) unlike it crosses the x-axis to the right of the resonant coordinate (at $x \approx 0.44\lambda$). This circumstance agrees with the behavior of $N_\perp^2$ presented in Fig. 5. Since $N_\perp^2 \to +\infty$ for $x \to +0$, the fast wave has a narrow propagation region to the right of the resonant point. It is this region which (in combination with the evanescent region in the fourth region) gives rise to the possibility of the localized ICRF signal studied in the present paper to exist. For $x < 0$, the wave field amplitude $H_z(x)$ decays with the distance from the resonance point but never turns to zero. Within the propagation region, $H_z(x)$ should spatially oscillate which means periodic turning to zero. Since the propagation region is narrow then one observes only one period of such oscillations.

In the fourth region, $x > \lambda$, the coupling between the fast and slow modes can be neglected. To determine the spatial distribution of the wave toroidal magnetic field one can apply eq. (6) which truncated form reads:

$$\frac{1}{k_0^2}\frac{d}{dx}\left(\frac{1}{N_\perp^2}\frac{dH_z}{dx}\right) + \frac{N_y}{k_0}\frac{d}{dx}\left(\frac{\mu}{N_\perp^2}\right)H_z = 0. \tag{24}$$

The term "$H_z \frac{N_y}{k_0}\frac{d}{dx}\left(\frac{\mu}{N_\perp^2}\right)$" in the l.h.s. of eq. (6) appears to be larger by the order of magnitude than "H_z" and "$-N_y^2 H_z/N_\perp^2$ due to strong change of the plasma density (9). This was also confirmed by numerical calculations. Solution of eq. (24) which satisfies the boundary condition of vanishing with going inside the plasma reads

$$H_z = A_4 \exp(-k_4 x). \tag{25}$$

In (25), $k_4 = \frac{\left(\sqrt{1+4\lambda k_y \omega/\omega_{ci}}-1\right)}{2\lambda} \approx \frac{k_y \omega}{\omega_{ci}} > 0$ with k_4^{-1} being the spatial scale at which the wave amplitude decreases by exp. For the plasma parameters applied in calculations for Fig. 7, $k_4 \approx 9.17\ m^{-1}$. It is even larger for the waves with $m = 5$: $k_4 \approx 34.03\ m^{-1}$, which means that the wave amplitude decreases by exp at the distance of $0.024\ m$.

The spatial distribution of the wave toroidal electric field can be found from eq. (5) which can be simplified in the fourth region as follows:

$$\frac{1}{k_0^2}\frac{d^2 E_z}{dx^2} + P E_z = 0. \tag{26}$$

The solution of eq. (26) which satisfies the boundary condition of vanishing with going inside the plasma reads

$$E_z = B_4 K_0\left(2\lambda\omega_{pe}/c\right). \tag{27}$$

For the plasma parameters applied in calculations for Fig. 7, the McDonald function argument in eq. (27) reads $1.872\exp(0.5x/\lambda)$.

IV. DISPERSION RELATION

In Section III, the wave field spatial distribution is derived with ten constants of integration. This means that application of the boundary conditions can result in the dispersion relation in the form of the ten-order determinant equal to zero. Such approach does not cause any numerical problems. However, on one hand, the ten-order determinant contains a lot of zero components. And on the other hand, the constants of integration A_{31}, A_{32}, B_{31} and B_{32} can be easily expressed in terms of A_1, B_1, B_{21}, and B_{22} which makes it possible to reduce the dispersion relation to the form with the six-order determinant equal to zero, $|a_{ij}| = 0$. This conversion does not cause any technical (mathematical) problems. Moreover, even this six-order determinant contains fourteen zero components. The components of the six-order determinant representing the dispersion relation are presented in Annex 1.

V. RESULTS OF NUMERICAL ANALYSIS OF THE DISPERSION RELATION

The dispersion relation is analyzed numerically by means of the standard package "Wolfram Mathematica", version 13.1 [23]. Some results are presented in Table 1. The code input includes the wave toroidal and poloidal indices,

Table 1. Eigen frequencies, Alfven refractive index squared in the resonance (1), $N_A^2(0)$, coefficient of proportionality between $N_A^2(0)$ and $(\omega/\omega_{ci})^2$

Toroidal wave index	Eigen angular frequency, ω/ω_{ci}	Eigen frequency, $\omega/(2\pi)$, MHz	$\frac{\omega_{pi}^2(0)}{\omega_{ci}^2}$	$\frac{N_A^2(0)}{(\omega/\omega_{ci})^2}$
1	1.855	27.063	0.83	0.241
2	3.562	51.959	3.34	0.263
3	5.308	77.437	7.50	0.266
4	7.062	103.026	13.34	0.267
5	8.819	128.653	20.84	0.268
6	10.577	154.301	30.02	0.268

plasma minor and major radii, and the plasma density decay length. ICRF normalized frequency ω/ω_{ci} is the code output.

Numerical solution of the dispersion relation is practically insensitive to the poloidal wave index value. The data for $n = 5{,}6$ is displayed in Table 1. However, the precision of the solutions (20)-(21) is unsatisfactory (44%) for $n = 5$, and it is even worse (76%) for $n = 6$. Assumption of existence of the sufficiently large evanescent region (fourth region) to the right of the resonance (1), where the fast wave decays with the distance from the resonance to the high-density plasma, fails for larger toroidal wave indices.

VI. CONCLUSIONS AND DISCUSSIONS

The following conclusions can be made from the presented analysis. First, the eigen frequencies are approximately proportional to the toroidal wave index, $\omega \propto |n|$. This feature is also known for Alfven waves. Consequently, the frequencies are almost equidistant. The eigen frequencies in Table 1 increase by about $\Delta\omega \approx 1.76\ \omega_{ci}$ with enhancing the toroidal wave index by a unit.

Second, the following question naturally arises when one scrutinizes the figures in Table 1: why the Table does not contain any data concerning the higher toroidal wave indices $n > 6$. The answer is that, first, for larger values of n (higher frequencies) the conditions of applicability of the applied approach worsen. Indeed, the change in the argument of exponential function in eq. (24), $k_4\Delta x$, within the evanescent region should be large. The local resonance (1) shifts to the denser plasma with increase of n, and the change $k_4\Delta x$ decreases. In particular, for chosen plasma parameters, this shift from the resonance position related to $n = 6$ to that related to $n = 3$ is $2.47\ cm$, while the distance between the H_z cut-off [28] position and the resonance position shortens from $7.48\ cm$ in the case of $n = 3$ to $2.71\ cm$ in the case of $n = 6$. And the second, the third term in the l.h.s. of eq. (6) should prevail over the first one to provide applicability of truncated eq. (24) in the fourth region. The following restriction can be derived from the latter condition:

$$\omega^3 \ll c^2\omega_{ci}/(a\lambda). \tag{28}$$

In (28), it is taken into account that $1 - N_z^2 \approx 0.27$ according to the data in Table 1 for all presented values of the toroidal wave indices. For the chosen plasma parameters, the r.h.s. of eq. (28) can be estimated as $\omega^3 \ll c^2\omega_{ci}/(a\lambda) \approx 1.7 \times 10^3\omega_{ci}^3$ or $\omega \ll 12.0\omega_{ci}$.

Third, it is assumed in the present paper that the RF signal is centered in the resonance (1), where

$$N_A^2(0) = (1 - N_z^2)(\omega^2/\omega_{ci}^2 - 1). \tag{29}$$

With taking into account that $\omega \propto |n|$ and hence $N_z^2 \approx Const = 0.72$ as well as $\omega^2 \gg \omega_{ci}^2$ one concludes from eq. (29) that the plasma particle density at the coordinate, where the RF signal is centered, should be almost proportional to the frequency squared, $n(0) \propto \omega^2$ (see the right column in Table 1). On one side, in this respect, numerical results agree with theoretical foresight. On the other side, this means that the coordinate, where the RF signal is predicted to be centered, varies with toroidal wave index n. If this variation is larger than the characteristic local resonance width, $\Delta x \sim (\rho_{Li}^2\lambda)^{\frac{1}{3}} \approx 5.3 \times 10^{-3}\ m$ [16,26,27], one should expect series of ICRF signals in a tokamak SOL, like it was reported in [21]. In the opposite case, ICRF signals spatially overlap and several frequencies should be registered in approximately one position with a nonzero width.

Fourth, the waves with negative poloidal wave indices, $m < 0$, do not contribute to the studied phenomenon. This is explained by the fact that the plasma is propagative for the fast magnetosonic waves with negative poloidal wave indices, $m < 0$, in the fourth region. From mathematical point of view, this conclusion results from the fact that both terms in eq. (24) are of the same sign in this case. This sign coincidence provides propagative character of the solution of eq. (24) which contradicts the initial assumption of the localized nature of the studied RF signal.

The numerical results were explained in [21] based on Fig. 3 in [21] as follows. Surface waves were suggested to arise in the evanescent region bordered by two propagative regions. Such structure is well-known from Quantum Mechanics (see e.g., [29]). The structure is called in Quantum Mechanics as “one-dimensional square potential barrier”. The wave function is well-known to fall from the left propagative region, reflect from the barrier and exponentially decay

within the evanescent region, and then the wave function propagates further into the right propagative region. To get localized increase of the wave amplitude (which is clearly seen in Fig. 13 in [21]), one needs the opposite structure: propagative region should be bordered by two evanescent regions. And just this structure was considered in [21]. The fast wave field spatial distribution was obtained there by the summation of the wave harmonics over k_z and k_y terms. For the wave harmonics with $k_y^2 + k_z^2 > k_0^2$, the left region (vacuum) is the evanescent region. Then a small propagative region takes place near Alfven resonance. And further there is an evanescent region to the right of Alfven resonance before the plasma density becomes sufficiently high and the plasma becomes propagative in the plasma core.

Mechanisms of RF signals' excitation are not discussed in the present paper. The problem of eigen values and eigen functions is considered only. Such signals can be excited either by ICRF antenna, by parametric decay or by energetic ion tails. At the same time, the suggested localized RF signal can still be considered as one of the mechanisms responsible for undesirable ICRF power absorption in the SOL.

Acknowledgement

Two of the authors are very thankful to Ukrainian Armed Forces for being alive. One of the authors is grateful to German people and in particular to IPP for the chance to live and work in Garching. Fruitful discussions with Drs. O. Girka and M. Usoltseva are highly appreciated.

Annex 1.

The components of the determinant a_{ij} which form the dispersion relation of the studied waves read:

$$a_{11} = a_{12} = 0,\ a_{13} = N_4 \equiv k_4/k_0,\ a_{14} = 1.0,\ a_{15} = N_z\omega/\omega_{ci},$$
$$a_{16} = -\omega_{pe}(0)N_z q K_1(q)/\omega_{ci},\ q = 2\lambda\sqrt{e(1-N_z^2)(\omega^2-\omega_{ci}^2)}/c, \quad (30)$$
$$a_{21} = a_{22} = 0,\ a_{23} = N_4 N_z\omega/\omega_{ci},\ a_{24} = a_{15},\ a_{25} = N_A^2(0)e,$$
$$a_{26} = -\omega_{pe}(0)a_{25}qK_1(q)/\omega, \quad (31)$$

$$a_{31} = \frac{N_z N_y}{1-N_z^2} - k_0\lambda N_y^2 N_z I_1,\ a_{32} = \frac{\sigma_1}{N_z^2-1} + \frac{N_z^2 N_y}{a_{25}}\frac{\omega}{\omega_{ci}}\sigma_2 + k_0\lambda\sigma_2 I_2,$$

$$a_{33} = 0,\ a_{34} = -\frac{N_z}{a_{25}}\frac{\omega}{\omega_{ci}},\ a_{35} = -1.0,\ a_{36} = 0, \quad (32)$$

$$a_{41} = -k_0^2\lambda^2 N_z I_3 + \frac{k_z\lambda N_y}{1-N_z^2} I_4 + k_0\lambda N_y N_z I_5 + k_1\lambda N_z I_6,$$

$$a_{42} = \frac{k_0\lambda\sigma_1}{N_z^2-1} I_4 - \sigma_2 - N_z^2 N_y\sigma_2 k_0\lambda I_6 + k_0^2\lambda^2\sigma_2 I_7,$$

$$a_{43} = a_{44} = a_{45} = 0,\ a_{46} = K_0(q), \quad (33)$$

$$a_{51} = 2k_0\lambda + k_0\lambda N_y^2 I_8 + \frac{N_1}{N_z^2-1},\ a_{52} = \frac{N_z N_y\sigma_2}{1-N_z^2} - N_y^2 N_z\sigma_2 k_0\lambda I_1,$$

$$a_{53} = a_{55} = 0,\ a_{54} = 1/a_{25},\ a_{56} = \omega_{pe}(0)N_z K_1(q)\sqrt{e}/(\omega_{ci}a_{25}) \quad (34)$$

$$a_{61} = 1 + k_0^2\lambda^2 I_9 + k_0^2\lambda^2 N_y^2 I_{11} - k_y\lambda I_{12} + \frac{k_1\lambda}{N_z^2-1} I_{13},\ a_{62} = 2N_y\sigma_2 k_z\lambda + N_z\sigma_1 k_0\lambda I_{12} + \frac{N_z k_y\lambda\sigma_2}{1-N_z^2} I_{13} - N_y^2 N_z\sigma_2 k_0^2\lambda^2 I_{14},$$

$$a_{64} = a_{65} = a_{66} = 0,\ a_{63} = -1. \quad (35)$$

The expressions for a_{32}, a_{42}, a_{52}, a_{62} contain the notations $\sigma_{1,2}$:

$$\sigma_1 = \frac{\xi_2}{k_0\lambda}\begin{Bmatrix} 0.5\xi_1[I_1(\xi_2)K_1(\xi_1) - I_1(\xi_1)K_1(\xi_2)] \\ +k_1\lambda[I_1(\xi_2)K_0(\xi_1) + I_0(\xi_1)K_1(\xi_2)] \end{Bmatrix}, \quad (36)$$

$$\sigma_2 = \xi_1[I_1(\xi_1)K_0(\xi_2) + I_0(\xi_2)K_1(\xi_1)] + 2k_1\lambda[I_0(\xi_2)K_0(\xi_1) - I_0(\xi_1)K_0(\xi_2)], \quad (37)$$

where the arguments of the Bessel functions read

$$\xi_1 = 2k_0\lambda\sqrt{\frac{1-N_z^2}{e}},\ \xi_2 = \frac{2\lambda\omega_{ci}}{c}\sqrt{N_A^2(0)\frac{m_i}{m_e}\frac{1-N_z^2}{e}}. \quad (38)$$

In (32)-(35), the definite integrals I_i read

$$I_1 = -\int_{-\lambda}^{\lambda}\frac{\mu}{N_\perp^2}d\left(\frac{x}{\lambda}\right), \quad (39)$$

$$I_2 = \int_{-\lambda}^{\lambda}\left(P - N_y^2 - \frac{N_z^2 N_y^2}{N_\perp^2}\right)d\left(\frac{x}{\lambda}\right), \quad (40)$$

$$I_3 = -\int_{-\lambda}^{\lambda}\left(\frac{1}{Q}\int_{-\lambda}^{x}\frac{\mu}{N_\perp^2}d\left(\frac{x}{\lambda}\right)\right)d\left(\frac{x}{\lambda}\right), \quad (41)$$

$$I_4 = \int_{-\lambda}^{\lambda}\frac{1}{Q}d\left(\frac{x}{\lambda}\right), \quad (42)$$

$$I_5 = -\int_{-\lambda}^{\lambda} \frac{1}{QN_\perp^2} d\left(\frac{x}{\lambda}\right), \tag{43}$$

$$I_6 = -\int_{-\lambda}^{\lambda} \frac{\mu}{QN_\perp^2} d\left(\frac{x}{\lambda}\right), \tag{44}$$

$$I_7 = \int_{-\lambda}^{\lambda} \left(\frac{1}{Q}\int_{-\lambda}^{x} \left(P - N_y^2 - \frac{N_z^2 N_y^2}{N_\perp^2}\right) d\left(\frac{x}{\lambda}\right)\right) d\left(\frac{x}{\lambda}\right), \tag{45}$$

$$I_8 = -\int_{-\lambda}^{\lambda} \frac{1}{N_\perp^2} d\left(\frac{x}{\lambda}\right), \tag{46}$$

$$I_9 = -\int_{-\lambda}^{\lambda} N_\perp^2 (1 + \frac{x}{\lambda}) d\left(\frac{x}{\lambda}\right), \tag{47}$$

$$I_{11} = \int_{-\lambda}^{\lambda} (N_\perp^2 \int_{-\lambda}^{x} \frac{1}{N_\perp^2} d\left(\frac{x}{\lambda}\right)) d\left(\frac{x}{\lambda}\right), \tag{48}$$

$$I_{12} = \int_{-\lambda}^{\lambda} \mu d\left(\frac{x}{\lambda}\right), \tag{49}$$

$$I_{13} = -\int_{-\lambda}^{\lambda} N_\perp^2 d\left(\frac{x}{\lambda}\right), \tag{50}$$

$$I_{14} = \int_{-\lambda}^{\lambda} (N_\perp^2 \int_{-\lambda}^{x} \frac{\mu}{N_\perp^2} d\left(\frac{x}{\lambda}\right)) d\left(\frac{x}{\lambda}\right). \tag{51}$$

All these integrals are dimensionless values. Some of the integrands, like in (47)-(51), are singular. For these integrals, Cauchy principal values should be taken. Imaginary parts of these integrals refer to the wave absorption and damping which are out of scope of the present paper as it is already mentioned above.

It is important to note the following significant difference between the case of exponential variation (9) of the plasma density used in the present paper and a linear one, $n_{lin} = n_0(1 + x/\lambda)$. If the variations of the numerators of the integral functions along x are neglected, the Cauchy principal value of integrals with linear variation of the resonant denominators within the symmetric limits is known to be equal to zero which is not the case for exponential variation of the resonant denominators. Indicated difference explains the absence of the wave field spatial distribution symmetry within the third region and consequently influences the dispersion relation.

ORCID

I. Girka, https://orcid.org/0000-0001-6662-8683; **O. Trush,** https://orcid.org/0000-0001-5105-2335
W. Tierens, https://orcid.org/0000-0002-6979-8140

REFERENCES

[1] H. Alfven, "Existence of electromagnetic – hydrodynamic waves," Nature, **150**(3805), 405–406 (1942). https://doi.org/10.1038/150405d0
[2] T.K. Allen, W.R. Baker, R.V. Pyle, and J.M. Wilcox, "Experimental generation of plasma Alfven waves," Phys. Rev. Letters, **2**(9), 383–384 (1959). https://doi.org/10.1103/PhysRevLett.2.383
[3] R. Betti, and J.P. Freidberg, "Ellipticity induced Alfven eigenmodes," Phys. Fluids B, **3**(8), 1865–1870 (1991). https://doi.org/10.1063/1.859655
[4] H.J.C. Oliver, S.E. Sharapov, B.N. Breizman, L.-J. Zheng, and JET Contributors, "Axisymmetric global Alfvén eigenmodes within the ellipticity-induced frequency gap in the Joint European Torus," Phys. Plasmas, **24**, 122505 (2017). https://doi.org/10.1063/1.5005939
[5] J. Candy, B.N. Breizman, J.W. Van Dam, and T. Ozeki, "Multiplicity of low-shear toroidal Alfvén eigenmodes," Physics Letters A, 215(5-6), 299-304 (1996).
[6] S. Mazzi, M. Vallar, U. Kumar, O. Krutkin, J. Poley-Sanjuan, L. Simons, J. Ball, S. Brunner, S. Coda, J. Garcia, A. Iantchenko, Ye.O. Kazakov, W.H. Lin, J. Ongena, B. Rofman, L. Villard, and the TCV team, "Study of fast-ion-driven toroidal Alfvén eigenmodes impacting on the global confinement in TCV L-mode plasmas," Front. Phys. Sec. Fusion Plasma Physics, **1**, 01-19 (2023). https://doi.org/10.3389/fphy.2023.1225787
[7] Y.I. Kolesnichenko, and A.V. Tykhyy, "Landau damping of Alfvénic modes in stellarators," Plasma Physics and Controlled Fusion, **60**(12), 125004 (2018). https://doi.org/10.1088/1361-6587/aae60a
[8] Ya.I. Kolesnichenko, Yu.V. Yakovenko, and M.H. Tyshchenko, "Mechanisms of the energy transfer across the magnetic field by Alfvén waves in toroidal plasmas," Physics of Plasmas, **25**(12), 122508 (2018). https://doi.org/10.1063/1.5049543
[9] V.S. Marchenko, S.N. Reznik, and Y.I. Kolesnichenko, "Nonlinear dynamics of multiple Alfvén modes driven by trapped energetic ions in tokamaks: A triplet paradigm," Physics of Plasmas, **31**(2), 022507 (2024). https://doi.org/10.1063/5.0186886
[10] V.E. Moiseenko, M.B. Dreval, Yu.V. Kovtun, Yu.S. Kulyk, G.P. Glazunov, Ye. O. Kazakov, J. Ongena, *et al*., "Fusion research in stellarator department of IPP NSC KIPT," PAST, 6, 3–8 (2022). https://doi.org/10.46813/2022-142-003
[11] M. Dreval, S.E. Sharapov, Ye.O. Kazakov, J. Ongena, M. Nocente, R. Calado, R. Coelho, J. Ferreira, A. Figueiredo, M. Fitzgerald, J. Garcia, C. Giroud, N.C. Hawkes, V.G. Kiptily, F. Nabais, M.F.F. Nave, H. Weisen, T. Craciunescu, M. Salewski, Ž. Štancar, and JET Contributors, "Alfvén cascade eigenmodes above the TAE-frequency and localization of Alfvén modes in D-3He plasmas on JET," Nuclear Fusion, **62**, 056001 (2022). https://doi.org/10.1088/1741-4326/ac45a4
[12] V.G. Kiptily, M. Fitzgerald, Ye O. Kazakov, J. Ongena, M. Nocente, S.E. Sharapov, M. Dreval, Ž. Štancar, T. Craciunescu, J. Garcia, L. Giacomelli, V. Goloborodko, H.J.C. Oliver, H. Weisen, and JET Contributors, "Evidence for Alfvén eigenmodes driven by alpha particles in D-3He fusion experiments on JET," Nuclear Fusion, **61**, 114006 (2021). https://doi.org/10.1088/1741-4326/ac26a2
[13] V. Kiptily, Ye. O. Kazakov, M. Nocente, J. Ongena, F. Belli, M. Dreval, T. Craciunescu, J. Eriksson, M. Fitzgerald, L. Giacomelli, V. Goloborodko, M.V. Iliasova, E.M. Khilkevitch, D. Rigamonti, A. Sahlberg, M. Salewski, A.E. Shevelev, J. Garcia, H.J.C. Oliver, S.E. Sharapov, Z. Stancar, H. Weisen, and JET Contributors, "Excitation of Alfvén eigenmodes by fusion-born

alpha-particles in D-3He plasmas on JET," Plasma Physics and Controlled Fusion, **64**, 064001 (2022). https://doi.org/10.1088/1361-6587/ac5d9e
[14] M. Vallar, M. Dreval, B. Duval, M. Garcia-Munoz, S. Sharapov, J. Poley-Sanjuan, A. Karpushov, P. Lauber, and TCV team, "Energetic particle modes in TCV with two neutral beam injectors," in: *Proc. 48th EPS Conference on Plasma Physics*, (2022). https://lac913.epfl.ch/epsppd3/2022/pdf/O4.110.pdf
[15] F. Rivero-Rodriguez, M. García-Muñoz, S. Sharapov, K. McClements, N. Crocker, M. Cecconello, M. Dreval, D. Dunai, M. Fitzgerald, J. Galdon-Quiroga, S. Gibson, C. Michael, J. Oliver, T. Rhodes, D. Ryan, L. Velarde, E. Viezzer, and MAST-U Team, "Experimental observations of fast-ion losses correlated with Global and Compressional Alfvén Eigenmodes in MAST-U," in: *Proc. 48th EPS Conference on Plasma Physics*. (2022). https://lac913.epfl.ch/epsppd3/2022/pdf/O4.109.pdf
[16] V.V. Dolgopolov, and K.N. Stepanov, "Cerenkov absorption of Alfvén waves and of fast magneto-acoustic waves in an inhomogeneous plasma," Nuclear Fusion, **5**, 276-278 (1965). https://doi.org/10.1088/0029-5515/5/4/003
[17] J. Vaclavik, and K. Appert, "Theory of plasma heating by low frequency waves: magnetic pumping and Alfven resonance heating," Nuclear Fusion, **31**(10), 1945-1997 (1991). https://doi.org/10.1088/0029-5515/31/10/013
[18] A.G. Elfimov, E.A. Lerche, R.M.O. Galvao, L.F. Ruchko, A.M.M. Fonseca, R.P. da Silva, and V. Bellintani, "Results of Localized Alfv´en Wave Heating in TCABR," Brazilian Journal of Physics, **34**(4B), 1707-1714 (2004). https://doi.org/10.1590/s0103-97332004000800036
[19] V.E. Moiseenko, Ye.D. Volkov, V.I. Tereshin, and Yu.S. Stadnik, "Alfvén resonance heating in Uragan-2M torsatron," Plasma Physics Reports, **35**(10), 828-833 (2009). https://doi.org/10.1134/S1063780X09100043
[20] I.O. Girka, "Fine structure of the local Alfven resonances in cylindrical plasmas with axial periodic inhomogeneity," in: *Problems of theoretical physics. Scientific works*, Issue 5. edited by V. O. Buts, (V.N. Karazin Kharkiv National University, Kharkiv, 2023). pp. 367-437.
[21] A. Messiaen, and V. Maquet, "Coaxial and surface mode excitation by an ICRF antenna in large machines like DEMO and ITER," Nuclear Fusion, **60**, 076014 (2020). https://doi.org/10.1088/1741-4326/ab8d05
[22] T.H. Stix, *Waves in Plasmas*, (American Institute of Physics, 1992).
[23] S. Wolfram, "Launching Version 13.1 of Wolfram Language & Mathematica," Stephen Wolfram Writings, (2022). https://writings.stephenwolfram.com/2022/06/launching-version-13-1-of-wolfram-language-mathematica/
[24] P.C. Stangeby, *The plasma boundary of magnetic fusion devices*, (Institute of Physics Publishing, 2000).
[25] I.O. Girka, and W. Tierens "Surface wave propagation along a narrow transition layer in a slab Voigt geometry," Physics of Plasmas, **31**, 022106 (2024). https://doi.org/10.1063/5.0182688
[26] I.A. Girka, and K.N. Stepanov, "Absorption and conversion of longwavelength fast magnetosonic waves in the region of local resonance in peripheral plasma," Ukrainian Journal of Physics, **35**, 1680-1688 (1990). (in Russian)
[27] I.A. Girka, V.I. Lapshin, and K.N. Stepanov, "Plasma heating near satellite Alfven resonances in stellarators," Plasma Physics Reports, **23**, 19-27 (1997).
[28] I.O. Girka, O.V. Trush, and W. Tierens, "Three different spatial positions of fast magnetosonic wave component turning points," Problems of Atomic Science and Technology. Series "Plasma Physics", 6, 86-91 (2024). https://doi.org/10.46813/2024-154-014
[29] A. Messiah, *Quantum Mechanics,* vol. 1 (North Holland Publishing Company, 1964).

ВЛАСНІ ВИСОКОЧАСТОТНІ СИГНАЛИ, ЛОКАЛІЗОВАНІ В ОКОЛІ АЛЬФВЕНОВИХ РЕЗОНАНСІВ ЗА ОСТАННЬОЮ МАГНІТНОЮ ПОВЕРХНЕЮ ТОКАМАКА

І. Гірка[a], О. Труш[a], В. Тіренс[b]
[a]Харківський національний університет імені В.Н. Каразіна, Харків, Україна
[b]Оук-Риджська національна лабораторія, Оук-Ридж, США

Розглянуто власні електромагнітні хвилі з малими тороїдними номерами моди та позитивними полоїдними номерами моди в іонному циклотронному діапазоні частот (ІЦДЧ). Теоретично показано, що існують хвилі у формі сигналів, локалізованих поблизу локальних Альфвенових резонансів (АР) за останньою замкненою магнітною поверхнею (ОЗМП) токамака. Просторове загасання в напрямку меншої густини плазми забезпечуються наявністю ненульових полоїдних номерів моди. Вузькі області просторового загасання в напрямку вищої густини плазми викликані сильною неоднорідністю плазми. Ці останні області відокремлюють АР від ОЗМП та центру плазми з високою густиною, який є областю поширення хвиль ІЦДЧ. Дисперсійне рівняння високочастотних сигналів виведено аналітично з застосуванням асимптотичних методів і розв'язано чисельно. Обговорено можливий зв'язок здобутих результатів з експериментальними вимірюваннями. Вичерпне визначення джерел збудження сигналів виходить за межі цього дослідження.

Ключові слова: *власні хвилі; іонний циклотронний діапазон частот; Альфвенів резонанс; остання замкнена магнітна поверхня токамака; асимптотичні методи; дисперсійне рівняння*